JOURNAL OF PROPULSION AND POWER
Vol. 22, No. 5, September–October 2006

Measurement of Vortices and Shock Waves Produced by Ramp and Twin Jets

Shunsuke Koike,* Kentaro Suzuki,† Eijiro Kitamura,* Mitsutomo Hirota,‡
Kenichi Takita,§ Goro Masuya,** and Masashi Matsumoto††
Tohoku University, Sendai 980-8579, Japan

Three-dimensional velocity distributions produced by a ramp injector in a Mach 2.35 airstream were measured with particle image velocimetry. Two jets were injected from the base of the ramp at Mach 2.0. Streamwise vorticity distributions were deduced from the velocity data, and their influence on the mixing of the twin jets was investigated. When the jets were not injected, a pair of counter-rotating vortices was observed behind the ramp. In contrast, two pairs of streamwise vortices could be observed when the jets were injected. The outer pair rotated in the same direction as the one produced by the ramp without injection, and their strength was intensified by the jets. The inner pair was weaker and rotated in a direction opposite to the outer pair.

Nomenclature

C_D = drag coefficient for sphere
d = diameter
M = Mach number
Re = Reynolds number
S = $M_{\mathrm{PF}}\sqrt{\gamma}/2$
T = temperature
t = time
U = velocity component in x direction
V = velocity component in y direction
W = velocity component in z direction
x = streamwise coordinate
y = spanwise coordinate
z = transverse coordinate
Δy = interval of grid in y direction
Δz = interval of grid in z direction
ε_v = uncertainty of velocity component in y direction
ε_w = uncertainty of velocity component in z direction
ε_{ω_x} = uncertainty vorticity component in x direction
λ = wavelength
μ = viscosity
ρ = density
ω_x = vorticity component in x direction

Subscripts

av = average
f = fluid
PF = relative value between particles and fluid
p = particle

Presented as Paper 2004-3656 at the AIAA 40th ASME/SAE/ASEE Joint Propulsion Conference and Exhibit, Fort Lauderdale, FL, 11–14 July 2004; received 4 August 2005; revision received 4 December 2005; accepted for publication 23 December 2005.

*Graduate Student, Department of Aerospace Engineering. Student Member AIAA.
†Graduate Student, Department of Aerospace Engineering; currently with Kanto Automobile Corporation.
‡Research Associate, Department of Aerospace Engineering.
§Associate Professor, Department of Aerospace Engineering. Senior Member AIAA.
**Professor, Department of Aerospace Engineering. Senior Member AIAA.
††Research Student. Department of Aerospace Engineering. Member AIAA.

I. Introduction

BECAUSE airflow in a scramjet engine combustor is very fast, injected fuel remains there for only very short time. Enhancement of fuel–air mixing is critically important for development of the scramjet engine. Development of turbulent shear layers is governed by the two-dimensional, large-scale vortex structure in subsonic flow. However, in supersonic flow, development of such a structure is inhibited by the compressibility effect.[1,2]

To enhance fuel–air mixing in supersonic flows, the introduction of streamwise vortices that are less affected by compressibility has been studied extensively.[3] For example, a ramp injector can introduce a pair of streamwise vortices and is rather easy to install on the combustor wall. Most ramp injectors in previous studies have injection holes at the ramp base.[4–6] On the other hand, the effect of the ramp located downstream of the injection hole was investigated also,[7] and this type of ramp arrangement was found to enhance the mixing efficiency.

The interaction between a light gas such as hydrogen and a shock wave is one of the most important issues for mixing enhancement in supersonic flow. These interactions produce vorticity by the baloclinic torque and enhance the mixing. Such effects were also studied in experimentally[8–10] and numerically.[9–11]

In the present research, a ramp injector with twin jets on its base is investigated. In Fig. 1, a typical flowfield around our ramp injector is shown. The shock wave emanating from the leading edge of the ramp produces the pressure gradient between the compression surfaces and the side of the ramp. The counter-rotating streamwise vortices produced by this pressure gradient enhance the mixing efficiency of the twin jets. Cutler and Johnson[6] also proposed a ramp injector with twin jets swirling from its base. Their twin jets, which were located very closely to one another, were expected to merge into a single jet whose surface velocity coincided with that of the airstream around it, thus reducing drag and increasing penetration. In contrast, we mainly focused on the effect of the interaction between the swirl in each jet and vortices produced by the ramp, as shown in a previous study.[12] When the swirls of the jets were in the same direction as those of the ramp vortices, the penetration of the injectant was improved. On the other hand, the injectant spread in the lateral direction when the direction of swirls was opposite to those of the ramp vortices.

In the previous experimental studies of the ramp injectors, measurements were made mainly for the two-dimensional distributions of the flowfield.[3–7,12,13] Donohue et al.[13] conducted one of the most detailed measurements around the ramp with a single jet using the planar laser-induced iodine fluorescence technique. In spite of

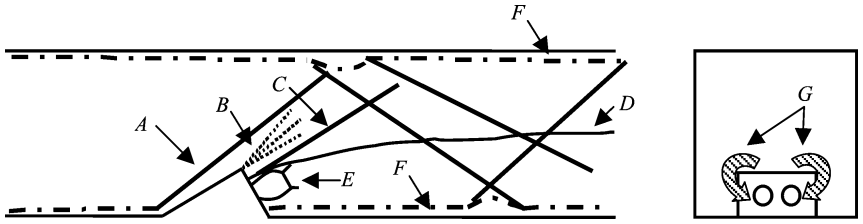

Fig. 1 Typical flow structure around ramp injector: A, shock wave emanated from leading edge of ramp; B, expansion wave from top of ramp; C, shock wave induced by jets; D, jet boundary; E, Underexpanded jet; F, boundary layer; and G, counter-rotating streamwise vortices.

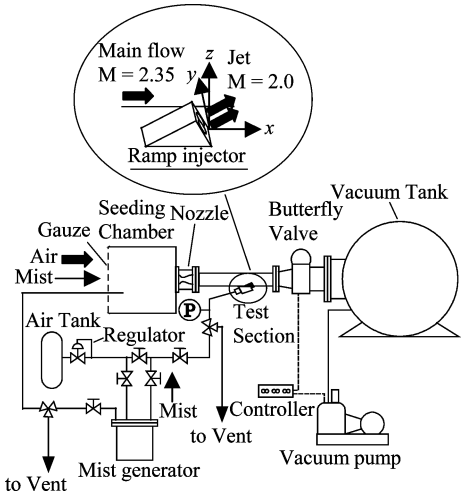

Fig. 2 Schematic of experimental setup.

these numerous studies, the three-dimensional characteristics of the flowfield around the ramp injector have not been determined because of difficulties with measurements. To clarify the phenomena observed in a previous study, it is important to obtain detailed information about the vortices produced by our ramp injector.

In the present research, three-dimensional velocity distributions around the ramp injector are assembled from two sets of two-dimensional velocity distributions measured with particle image velocimetry (PIV). The streamwise vortices produced by the ramp with and without injection are identified from the velocity distributions and the function of those streamwise vortices are discussed. There are two reasons that we measure the two cases. One is to clarify the characteristics of vortices interacting with swirls in previous research. Another is to clarify the influences of the twin jets on the streamwise vortices. In a scramjet engine combustor, injection positions are changed as the flight Mach number changes to control the combustion mode. There may appear ramps without injection sometime during flight. It is important to obtain such information in such a case as well.

II. Experiment Apparatus and Methods

A. Test Facility

The experiment apparatus is shown schematically in Fig. 2. A suction-type, supersonic wind tunnel was used. Unheated atmospheric air was inhaled into a vacuum tank through a two-dimensional contoured nozzle and a test section. The tank had a volume of 8 m^3 and was evacuated to about 5 kPa before each run. A chamber was set at the entrance of the nozzle to seed tracer particles into the air for PIV measurement. The test section had a 30 mm^2 cross section and was 330 mm long. The nominal Mach number of the airstream was 2.35, and the duration of each run was about 25 s. The unit Reynolds number was 1.13×10^7 1/m. The boundary layer of the test section was turbulent. A ramp injector was attached to a wall of the test section 225 mm downstream from its entrance. The other three walls of the test section had glass windows for PIV measurement.

The injectant was pressurized air fed from a tank. Tracer particles were also supplied to the injectant line. The ramp injector is shown in Fig. 2. The ramp injector was same as that in previous research[12] and was an unswept type with a 30-deg compression surface. The trailing edge of the compression surface was 12 mm wide and 5.2 mm high from the tunnel wall. The size of the ramp was determined considering the resolution of the measurement technique. For example, because the resolution of PIV system in the present study was 1 mm, if the size of the ramp was too small, the characteristic of the velocity field became too small to resolve. The ramp base was canted at 60 deg. There were two conical, converging–diverging nozzles on the ramp base for injection. The diameters of throat and exit of each injector nozzle were 2.7 and 3.5 mm, respectively. The distance between the nozzle axes was 7 mm. The Mach number of the injector nozzle calculated from the area ratio assuming isentropic flow was 2.0. The axes of the nozzles were parallel to each other and the injection angle was 30 deg to the main stream. The nozzle for the main stream was designed to produce Mach 2.5 flow. The ramp angle of 30 deg is the maximum value of the oblique shock wave in Mach 2.5 flow that does not detach from the leading edge of the ramp. To produce the strongest vortex in Mach 2.5 flow, 30 deg were selected. Although each jet can be swirled by tangentially introducing the injectant to a cylindrical chamber set in the upstream of the nozzle, only the straight (nonswirling) jets were injected in the present experiment.

The mass flow rate of the injectant was measured with a choked orifice. Total temperature and total pressure upstream of the orifice were measured with a thermocouple and a strain-gauge pressure transducer. The ratio of the momentum flux of the jet at the nozzle exit to that of the main stream was estimated at 1.36 by assuming an isentropic flow.

A Cartesian coordinate system (Fig. 2) is used in this paper. The origin is at the intersection of the centerline of the wall and the ramp base plane. The streamwise axis is x, the spanwise axis y, and the transverse axis z.

B. Pressure and Temperature Measurements

Strain-gauge pressure transducers (Omegadyne, Inc., PX5503L0-015AV and Kyowa, Inc., PGM20KH) were used to measure the injectant total pressure and the wall pressures in the test section. The signal from each transducer was amplified by a dc amplifier (NEC, Inc., AS2102), digitized by a 14-bit A/D converter, and recorded by a data recorder (Keyence, Inc., NR2000). The accuracy of the pressure measurement system was estimated as $\pm 1\%$. Temperature was measured with a K-type thermocouple. Its signal was digitized by a 16-bit A/D converter and recorded by the data recorder (Keyence, Inc., NR1000).

C. PIV System

1. Optics and Analysis System

A double-pulsed Nd:YAG laser (TSI, Inc., $\lambda = 532$ nm, 12 mJ/pulse, pulse duration 5–7 ns, Y12-15E) was used as a light source. A mirror and two cylindrical lenses were used to produce a laser sheet about 0.5 mm thick and 50 mm wide. The error in positioning the laser sheet relative to the test section was less than ± 0.2 mm

Because the flow was supersonic, the tracer particles might pass through the laser sheet in the interval between laser pulses if the laser sheet was introduced perpendicular to the main flow. Thus, the plane that contains the velocity vectors of the undisturbed main

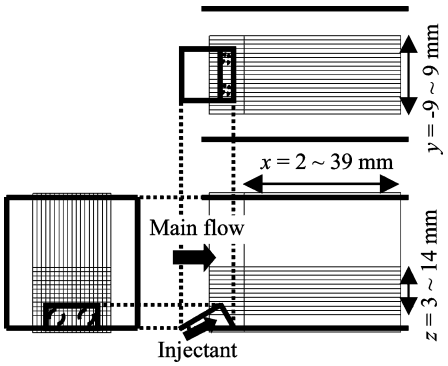

Fig. 3 Field of PIV measurements.

stream was illuminated with the laser sheet and measured. The test section was turned 90 deg around its center axis to measure the velocity fields in the x–y and x–z planes. The velocity fields in the y–z cross sections were constructed from the x–y and x–z plane data.

The light scattered by tracer particles in the flow was recorded with a charge-coupled device (CCD) camera (TSI, Inc., 1280 × 1024 pixels, PIV13-8). An interference filter was attached to the lens of the camera to block the light reflected from the wall surface that was covered with a film to shift the wavelength of the reflected light. The particle images were recorded in the double-frame, single-exposure mode of the PIV system. The laser and the CCD camera were synchronized with a synchronizer (TSI, Inc., Model 610034). The separation time of the successive laser pulses was 400 ns. The visualization image data were transferred to a personal computer for processing to calculate the two-dimensional velocity vectors in the plane of the laser sheet using the cross-correlation method with an analyzing program (TSI, Inc., INSIGHT3.32).

To determine the number of image pairs required to measure the objective flowfield, preliminary experiments with an underexpanded sonic jet from a converging nozzle were performed. There were 1000 pairs of pictures taken and processed using the method described hereafter. The changes in average velocity vectors were investigated by changing the number of processed picture pairs. This preliminary investigation indicated that 350 picture pairs were required to achieve convergence within ±2% of the averaged velocity data obtained with 1000 pairs.

The planes where velocities were measured with PIV are shown in Fig. 3. These were the x–y planes from $z = 3$ to 14 mm and the x–z planes from $y = -9$ to 9 mm at intervals of 1 mm. The required 350 pairs of photographs were taken for every plane. The field of view was 55.7 × 44.5 mm, and the resolution of the recording was 43.5 μm/pixel.

Because of the mist-covered window, the reflected light from the wall, and the shortage of particles, erroneous vectors appeared in the data. It was necessary to eliminate these erroneous vectors. In addition, if the number of erroneous vectors were more than a specified value at certain measurement points, such a point would be classified as an invalid. In this experiment, the elimination of the erroneous vectors and the classification of the invalid measurement points were carried out with the following postprocesses.

First, the average and the standard deviation of the velocity vector at each point were calculated from the whole output of the PIV software. Then the data whose difference from the averaged value in each component were smaller than the standard deviations were adopted as valid.

After these postprocesses on each vector datum, the measurement points were classified. The number of adopted data differed at each point because of the data selection just mentioned. We consider the average velocity obtained by the adopted data at each point to be reliable only when the number of adopted data exceeds 25% of all of the data (350 data). Points whose data set did not satisfy this criterion were classified as invalid. The 25% threshold was determined to include as valid the points close to a Mach disk, where large fluctuations occurred.

2. Tracer Particles

The tracer particles for the PIV measurement were droplets of dioctyl sebacate (density 913.5 kg/m^3) produced with Laskin nozzles (see Ref. 14) in a mist generator. This generator was designed to supply mist to the flow feed line pressurized up to 3 MPa.

The response of the tracer particles to the change of flow velocity is very important for the PIV measurement, and particle diameter strongly affects this response. Therefore, we conducted preliminary experiments to examine the response of the tracer particles passed through a Mach disk produced by an underexpanded jet ejected from a converging nozzle.[15] The diameter of the nozzle exit was 6.5 mm. A swirler[15] could be attached in the converging part of the nozzle, but it was not used in this test of tracer particle response. The jet was ejected into a quiescent atmosphere. Static pressure at the nozzle exit was estimated to be 2.7 times the atmospheric pressure from the measured feed pressure and the isentropic relation. The total temperature of the jet was 280 K.

The motion of the tracer particles was described by the following equation:

$$\frac{\mathrm{d}U_p}{\mathrm{d}t} = -\frac{3}{4}C_D\frac{\rho_p}{\rho_f}\frac{1}{d_p}(U_p - U_f)^2 \tag{1}$$

Here, C_D is the drag coefficient for a sphere. In a low-speed flowfield, the relative velocity between tracer particles and fluid is small for PIV, and so the Stokes law can be used for the drag coefficient. However, in our experiment, the relative velocity behind the Mach disk exceeded 400 m/s. The Reynolds number with relative velocity and the diameter of the particle was, thus, 163, assuming a particle diameter of 1.0 μm. In addition, the Mach number of the relative velocity was 1.3. Because both Reynolds and Mach numbers exceeded the ranges where Stokes's or Oseen's law for incompressible flow was applicable, both the high Reynolds number and compressibility effects should be considered for the drag coefficient in Eq. (1). Henderson[16] proposed the following drag coefficient, taking into account compressibility and the temperature difference between the solid particles and fluid as well as the Reynolds number relative value between particles and fluids. In the subsonic region ($M_{\mathrm{PF}} < 1$), the drag coefficient is written as

$$C_D\left(M_{\mathrm{PF}}, Re_{\mathrm{PF}}, \frac{T_p}{T_f}\right) = 24\left(Re_{\mathrm{PF}} + S\left\{4.33 + \left[\frac{3.65 - 1.53(T_p/T_f)}{1 + 0.353(T_p/T_f)}\right]\exp\left(-0.247\frac{Re_{\mathrm{PF}}}{S}\right)\right\}\right)^{-1} + \exp\left(-\frac{0.5M_{\mathrm{PF}}}{\sqrt{Re_{\mathrm{PF}}}}\right)\left[\frac{4.5 + 0.38(0.03Re_{\mathrm{PF}} + 0.48\sqrt{Re_{\mathrm{PF}}})}{1 + 0.03Re_{\mathrm{PF}} + 0.48\sqrt{Re_{\mathrm{PF}}}} + 0.1M_{\mathrm{PF}}^2 + 0.2M_{\mathrm{PF}}^8\right] + \left[1 - \exp\left(-\frac{M_{\mathrm{PF}}}{Re_{\mathrm{PF}}}\right)\right]0.6S \tag{2}$$

and for the supersonic region ($M_{\mathrm{PF}} > 1.75$),

$$C_D\left(M_{\mathrm{PF}}, Re_{\mathrm{PF}}, \frac{T_p}{T_f}\right) = \left\{0.9 + \frac{0.34}{M_{\mathrm{PF}}^2} + 1.86\left(\frac{M_{\mathrm{PF}}}{Re_{\mathrm{PF}}}\right)^{\frac{1}{2}}\left[2 + \frac{2}{S^2} + \frac{1.058}{S}(T_f/T_p)^{\frac{1}{2}} - \frac{1}{S^4}\right]\right\} \Big/ 1 + 1.86\left(\frac{M_{\mathrm{PF}}}{Re_{\mathrm{PF}}}\right)^{\frac{1}{2}} \tag{3}$$

where

$$S = M_{\mathrm{PF}}\sqrt{\gamma/2} \tag{4}$$

In the Mach number region between 1 and 1.75, the drag coefficient is linearly interpolated using the following equation:

$$C_D(M_{\mathrm{PF}}, Re_{\mathrm{PF}}, T_p/T_f) = C_D(1.0, Re_{\mathrm{PF}}, T_p/T_f) + \tfrac{4}{3}(M_{\mathrm{PF}} - 1.0) \times [C_D(1.75, Re_{\mathrm{PF}}, T_p/T_f) - C_D(1.0, Re_{\mathrm{PF}}, T_p/T_f)] \tag{5}$$

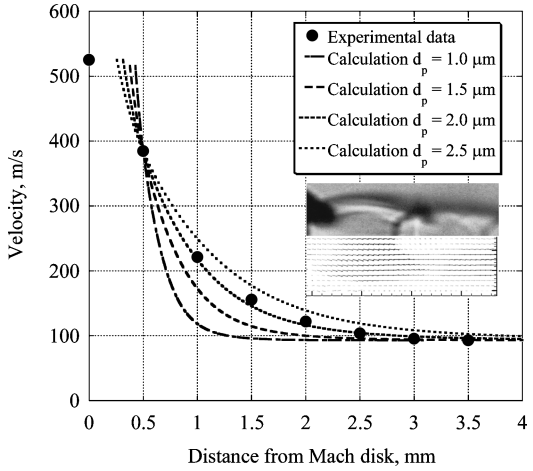

Fig. 4 Response of tracer particles in passing through Mach disk.

where $C_D(1.0, Re_{\mathrm{PF}}, T_p/T_f)$ represents the coefficient calculated using Eq. (2) with $M_{\mathrm{PF}} = 1$, and $C_D(1.75, Re_{\mathrm{PF}}, T_p/T_f)$ represents the coefficient calculated using Eq. (3) with $M_{\mathrm{PF}} = 1.75$. Henderson[16] compared experimental data with his equations for the range of $M_{\mathrm{PF}} \leq 6$ and $Re_{\mathrm{PF}} \leq 10^4$, and reported that the maximum deviation was 16%.

Figure 4 shows the axial velocity distributions on the nozzle centerline downstream of the Mach disk. The solid circles are the PIV data, and the lines are data calculated from Henderson's[16] equations with $T_f/T_p = 1$ and different particle sizes. In this experiment, the temperature of the particles and the fluid behind the Mach disk were almost that of the atmospheric air, and so $T_f/T_p = 1$ was adopted. Because the position of the Mach disk was between $x = 0$ and 0.5 mm, in Fig. 4 the lines were fitted the experimental data at $x = 0.5$ mm, the first data behind the Mach disk. Comparison between the experimental data and the calculated curves indicated that the particle diameter was about 2.0 μm. This is a little larger than that obtained by Kitamura et al.[17] with the gravitational sedimentation method.

For this particle diameter, the characteristic delay time (the time required to reduce velocity difference to $1/e$ of the initial value in the stepwise change) was estimated to be 12.8 μs when the particles pass through an oblique shock wave inclined 40 deg to the mainstream of a Mach 2.35 flow. In this estimation, the Reynolds number relative value between particles, and fluids just behind the shock wave was 9.8. This result means that it needed to be 7.9 mm normal to the oblique shock wave for the tracer particles to follow the normal velocity component with less than 10% error.

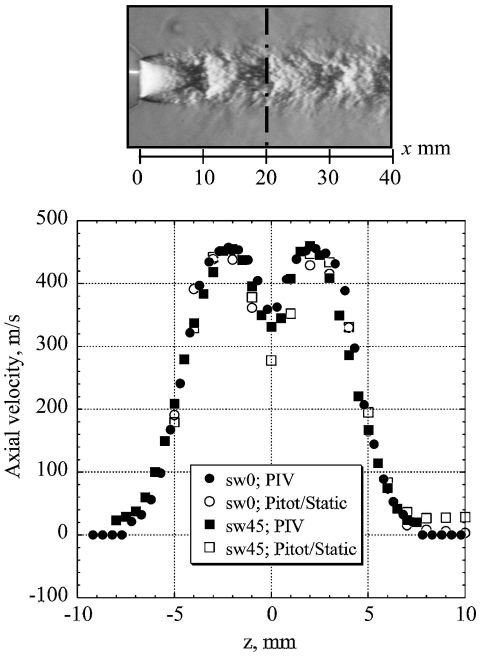

Fig. 5 Axial velocity distributions of single freejet by PIV and pitot/static pressure probe at $x = 20$ mm.

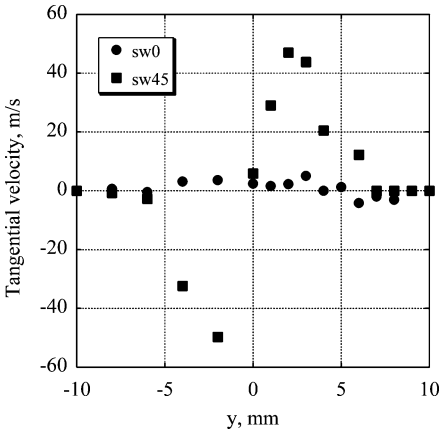

Fig. 6 Tangential velocity distributions of single freejet without swirl (sw0) and with swirl (sw45) at $x = 20$ mm.

D. Accuracy of Supersonic Velocity and Streamwise Vorticity

To confirm the applicability of the PIV system used in the present study to the supersonic flow with streamwise vortices, one of two swirlers, sw0 or sw45, was attached in the converging nozzle. Vanes of the sw0 swirler did not incline to the nozzle axis, and they added no swirl to the flow. However, the vanes of the sw45 swirler inclined 45 deg to the nozzle axis added a swirling component to the flow velocity. The supersonic jet was ejected into the quiescent atmosphere. The tracer particles were fed only to the supersonic jet. Figure 5 shows a comparision of the radial distributions of the axial velocity component at $x = 20$ mm measured by the PIV and a pitot/static pressure probe. The distributions of the two methods agree very well, except for the data near the axis in the case with the sw45 swirler. This result demonstrates that the PIV system was an appropriate method to measure the mean velocity of supersonic airflow as high as 500 m/s.

The tangential velocity component was obtained by shifting the laser sheet away from the nozzle axis. Figure 6 shows the distribution of the tangential velocity component measured by the PIV with the sw0 and sw45 swirlers. As expected, the tangential velocity components for the sw0 swirler were almost zero. In the sw45 case, a forced-vortex velocity profile was seen near the centerline and a free-vortex profile was seen far from the central region. The maximum value of the tangential component was about 50 m/s in this section. The tangential movement of the particle between the two laser pulses in this case was less than 20 μm, and this is only 4% of the thickness of the laser sheet.

The theoretical angular momentum was calculated at the swirler exit assuming that the axial velocity could be obtained from the quasi-one-dimensional isentropic relation and that the flow was parallel to the swirler vane. The angular momentum was 6.4×10^6 Nm with the sw45 swirler installed. Those in the sections of $x = 10$, 20, 30, and 40 mm were calculated by numerically integrating the velocities measured with the PIV and the densities calculated from static pressure data. The average angular momentum was 3.8×10^6 Nm, about 60% of the theoretical value. The disagreement of the theoretical and measured values was mainly caused by viscous loss in the nozzle. The measured angular momentums were conserved within $\pm 28\%$ in the flow.

To describe the information on the streamwise vortices, the vorticity component in the x direction will be calculated in the next section. Thus, it is important to estimate the uncertainty of the vorticity component in the x direction. Vorticity is calculated using the second-order central difference. In this case, the uncertainty of

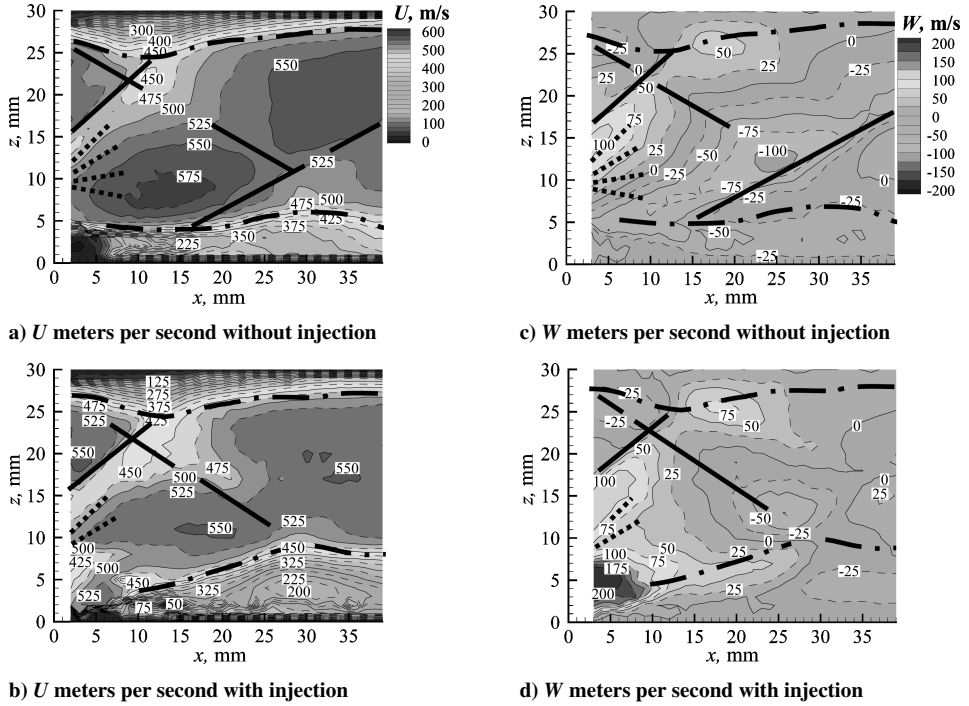

a) U meters per second without injection

c) W meters per second without injection

b) U meters per second with injection

d) W meters per second with injection

Fig. 7 Contours of streamwise and transverse velocity components in x–z plane of $y = -4$ mm: ——, Shock wave; · · · ·, expansion wave; and —·—, boundary layer.

vorticity depends on those of the velocity components v and w, the length of the grids Δy and Δz, and higher-order terms of Δy and Δz. Among these three factors, the term depending on the uncertainty of the velocity components v and w was much larger than the others. Thus, only the uncertainty that depends on the velocity components is estimated here. It is calculated via the next equation, considering Δy and Δz the same and assuming that the uncertainty of v and w on the neighboring grid was same,

$$\varepsilon_{\omega_x} = \left(1/\sqrt{2}\Delta y\right)\sqrt{\varepsilon_v^2 + \varepsilon_w^2} \tag{6}$$

Here, ε and ω_x indicate the uncertainty and vorticity component in the x direction, respectively. To estimate the uncertainty of v and w, the difference of the result measured with PIV and a pitot/static pressure tube in the case without swirl, shown in Fig. 5, were referred to. In this case, the maximum and the average errors of the PIV data were 17.5 and 6.5%, respectively, assuming that the results measured with pitot/static pressure tube were of the true value. In the region measured with PIV, the maximum values of v and w are almost 100 m/s. Thus, the maximum and average uncertainty of v and w are estimated 17.5 and 6.5 m/s, respectively. Given these values and that the distance between the grids was 1 mm, the maximum and average values of uncertainty for the value 50,000 1/s was estimated as 1.2×10^4 and 4.6×10^3 1/s, or 24 and 9%, respectively. Three-dimensional surface contours at 50,000 1/s will be shown in the next section.

III. Results and Discussion

A. Velocity Components on x–z Plane

Averaged magnitudes of streamwise and transverse velocity components, U and W, respectively, in the $y = -4$ mm plane are shown in Fig. 7 for the cases with and without injection. This plane is 0.5 mm outside the center of the injection nozzle. In Fig. 7, the lines that indicate a shock wave, expansion wave, and boundary layer are shown. Under both cases with and without injection, we can clearly see that an oblique shock wave generated by the ramp (from $x = 2$ mm and $z = 15$ mm to $x = 11$ mm and $z = 25$ mm) rapidly decelerated and deflected the flow. This oblique shock wave impinged on the boundary layer of the upper wall. The boundary layer thickened due to the shock-wave boundary-layer interaction. The reflected wave was less clear than the incident one.

In the noninjecting case, the flow behind the oblique shock wave was reaccelerated and deflected downward by an expansion fan that emanated from the trailing edge of the ramp at $x = -3.0$ mm and $z = 5.2$ mm. Actually, W became negative in a wide region, and U around $x = 13$ mm and $z = 8$ mm was about 50 m/s higher than the undisturbed freestream. The low-speed region at the lower left corner of Figs. 7a and 7c was a recirculation zone behind the ramp. The recompression shock wave can be seen from $x = 15$ mm and $z = 4$ mm to $x = 30$ mm and $z = 10$ mm, where it crossed with the reflected shock wave from the upper wall. This recompression shock wave turned the main flow parallel to the lower wall again. The oblique shock wave reflected by the upper wall propagated into the region near the lower wall. The flow was deflected downward and decelerated by this shock wave.

With injection, the expansion wave from the ramp edge was seen only above the jet in this plane. The z components had large positive values near the ramp. The x components were high and almost the same speed as the main flow near the injection hole ($x = 5$ mm and $z = 3$ mm). This result indicates that the shear stress produced by the difference of speed between the main flow and the jets was low, and strong mixing of the injectant was not expected to be caused by the shear. The boundary layer on the lower wall was thickened by impingement of the reflective shock wave from the upper wall. This effect appeared more significantly in the injection case than in the noninjection case.

B. Velocity Components on x–y Plane

Contours of U and V in the $z = 6$ mm plane are shown in Fig. 8. This plane lay slightly above the trailing edge of the ramp. Note that the velocity was measured only in the central two-thirds of the duct width because of the size of the window attached to the upper wall. In the noninjecting case, a long elliptic region of low-speed (A) in Fig. 8a was produced by the recompression shock wave and the reflected shock waves from the upper wall and the sidewalls. The width of the low-speed region was almost the same as that of the ramp. In the lateral velocity distributions shown in Fig. 8c, strong outward flows were observed on both sides of the ramp, but they disappeared as the flow went downstream of the ramp base. The central region around $x = 25$ mm was decelerated by the recompression shock wave, and the flow was moving outward.

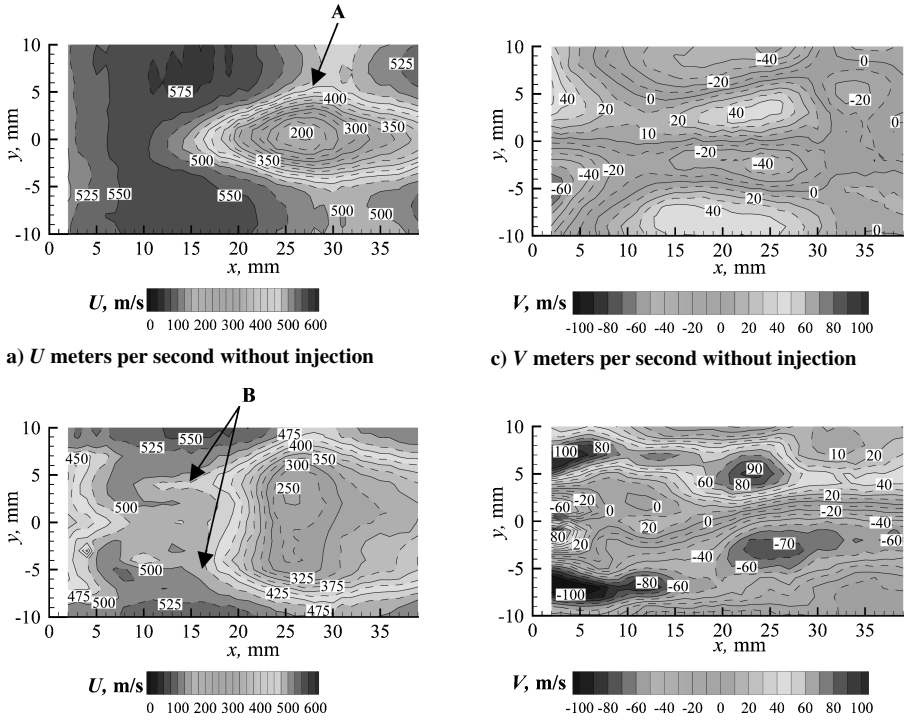

a) U meters per second without injection

c) V meters per second without injection

b) U meters per second with injection

d) V meters per second with injection

Fig. 8 Contours of streamwise and spanwise velocity components in x–y plane of $z = 6$ mm.

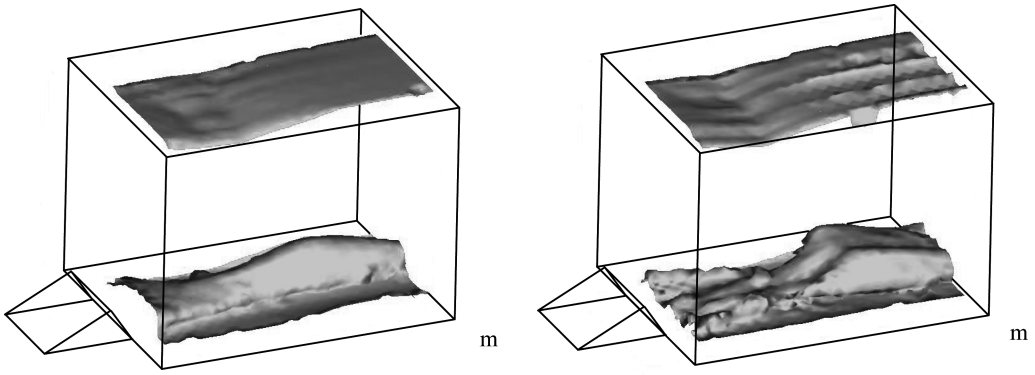

a) Without injection

b) With injection

Fig. 9 Isovalue surface of $U = 300$ m/s.

The width of the low-speed region for the injection case exceeded that for the noninjection case. Beneath each jet ($y = \pm 4$ mm), there appeared a narrow low-speed band (B) extending upstream from the decelerated region. It was considered that this extended low-speed region appeared because the jets decelerated by the Mach disk produced the low-speed region and the main airstream that was high speed could not flow near the lower wall because of the existence of the jets. Near the ramp base, the lateral expansion of the jets turned the airstreams on both sides of the ramp outward. In the central part of the ramp base region, each of the twin jets restricted the expansion of the other jet and resulted in a small absolute value of V. At approximately $x = 20$ mm, strong outward flows were observed from the central low-speed, high-pressure flow produced by the reflected shock. Because the twin jets supplied sufficient volumetric flow to fill the space behind the ramp base, the inward flows near the sidewalls that appeared in the noninjection case were not observed in the injection case.

C. Velocity Component in x Direction

Contour surfaces of $U = 300$ m/s are shown in Fig. 9 for the noninjection and injection cases to show the three-dimensional features of the low-speed region. Note that these surfaces do not represent any stream surfaces. In the former case, the cross section of the low-speed region bounded by the contour surface near the ramp injector resembled the base of the ramp. As it moved downstream, it first converged due to the inflows accelerated by the expansion waves from the trailing edges of the ramp. The low-speed region then expanded because of the formation of the recompression shock wave and the incidence of reflection shock wave and had a single peak at around $x = 25$ mm and $y = 0$ mm.

In the injection case, two ridges of the low-speed region were seen below the twin jets. These two ridges became large and high because of the incidence of the reflection shock wave from the upper wall. Two peaks appeared in the low-speed contour surface, indicating that the low-speed ridges under the jets continued downstream. The width of the low-speed region with injection exceeded that without injection.

Figure 10 shows the distributions of the streamwise velocity component U in the cross sections at $x = 5$, 8, and 10 mm for the injection case. In the $x = 5$ mm section, there were two low-speed regions, one at the midheight ($z \cong 15$ mm, A) and the other around the twin jets (B). The former was a region between the shock wave from the leading edge of the ramp and the expansion fan from the trailing edge of the ramp. The latter was the separated boundary layer on the ramp surface. There was a local maximum value of U near the center

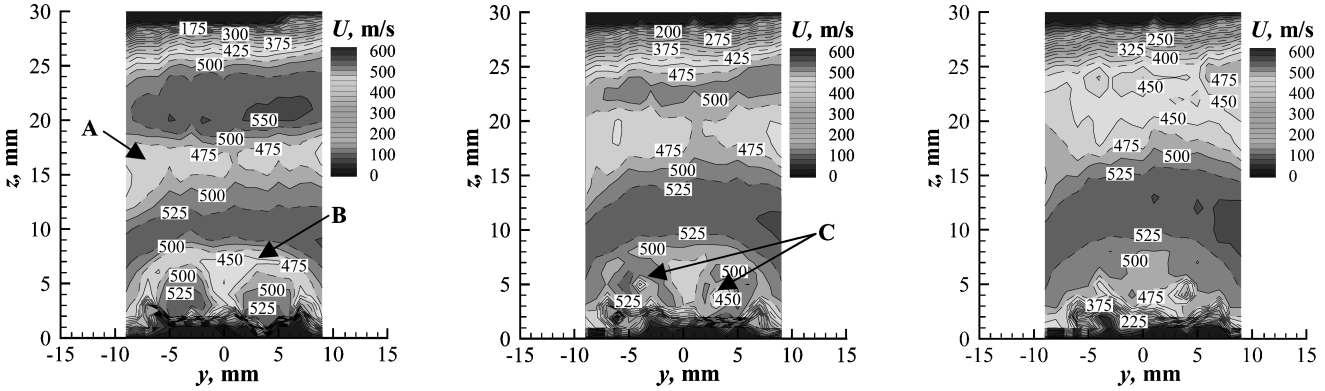

a) $x = 5$ mm b) $x = 8$ mm c) $x = 10$ mm

Fig. 10 Cross-sectional distribution of streamwise velocity component U meters per second with injection.

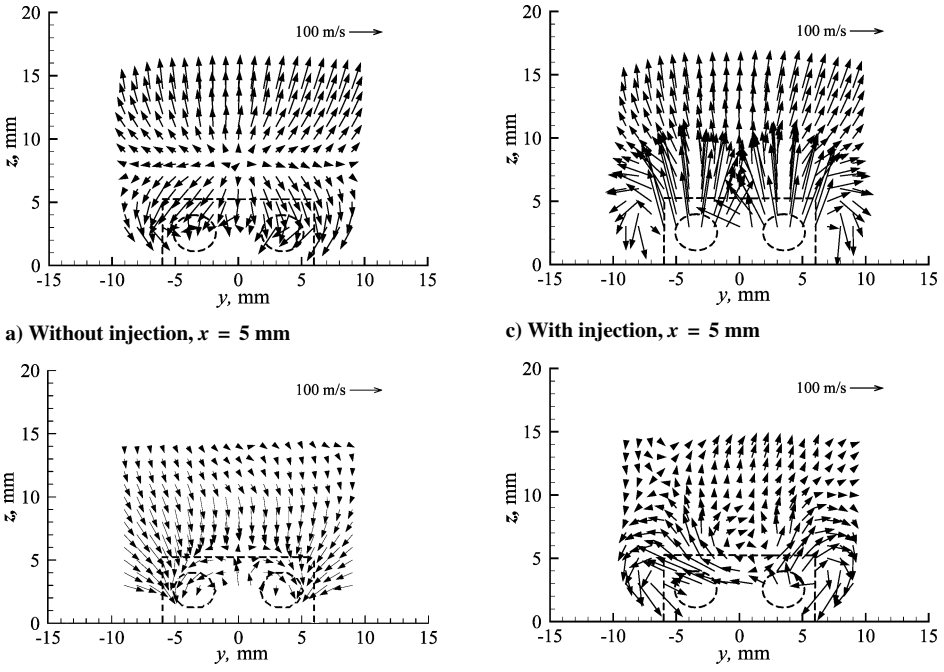

a) Without injection, $x = 5$ mm c) With injection, $x = 5$ mm

b) Without injection, $x = 15$ mm d) With injection, $x = 15$ mm

Fig. 11 Streamwise development of cross-sectional velocity vector fields.

of each jet ($y = \pm 4$ mm and $z = 3$ mm, C). However, in the $x = 8$ mm section, the central region of each jet became a local minimum surrounded by a high-speed region. The jets became overexpanded, and shock waves were formed in the jets, decelerating their central parts between $x = 5$ and 8 mm. The side view of this decelerating process can be seen in Fig. 7b at $x = 7$ mm and $z = 5$ mm. Also note that the low-speed region under the jets in the $x = 8$ mm section became thicker than that in the upstream section. The two low-speed ridges mentioned earlier corresponded to these low-speed cores of the jets. The lower part of the high-speed region around the core was decelerated by the low-speed boundary layer. At $x = 10$ mm, the local high-speed region around the jets could not be seen.

D. Vortex

The velocity data of the x–z planes and the x–y planes were compounded to determine the velocity vectors in the y–z cross sections. Those in the $x = 5$ and 15 mm cross sections are shown in Fig. 11. In Fig. 11, the rectangle and ellipses represent the ramp injector projected in the y–z plane.

In the noninjection case, the vectors in the $x = 5$ mm section at the level of the ramp surface moved outward from the center of the ramp surface because of the pressure difference between the ramp surface and the sides of the ramp. In contrast, the flow near the lower wall went to the center of the ramp. This indicates that a pair of the counter-rotating vortices was rolling up at both sides of the ramp. The vortex pair was clearly seen in the $x = 15$ mm section.

In the injection case, we can see strong expansion of each jet around its injection port at $x = 5$ mm. Because the jets prevented the main flow from moving into the base region of the ramp injector, the main flow was forced to spread in the lateral direction more strongly and widely than that in the noninjection case. An intensified vortex pair, whose centers were pushed outside of the ramp sidewalls, was formed at the cross section of $x = 15$ mm. The shape of each vortex looked like a flattened circle.

Vorticity distributions were calculated from the averaged velocity data to visualize the location and development of the streamwise vortices. The second-order central difference was used to calculate the velocity gradient except for boundary points where the first-order one-sided difference was used.

The distributions of the streamwise vorticity component in the y–z and x–y planes can be seen in Figs. 12 and 13, respectively. Figure 14 presents the three-dimensional views of the contour surface of streamwise vorticity. Only the surfaces of ± 50000 1/s are shown for clarity.

In the noninjection case, a pair of contoured surfaces with the same magnitude of vorticity in the opposite sign existed from $x = 10$ to 30 mm as shown in Figs. 12a, 12b, and 14a. They corresponded

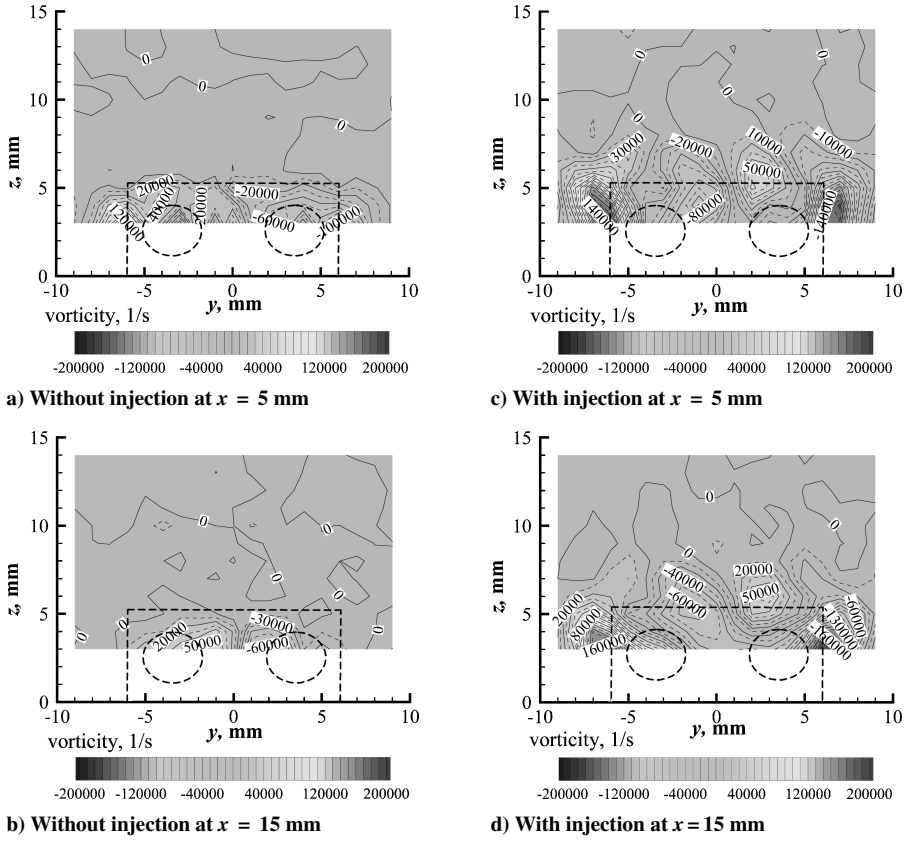

a) Without injection at x = 5 mm

c) With injection at x = 5 mm

b) Without injection at x = 15 mm

d) With injection at x = 15 mm

Fig. 12 Contours of vorticity component in x direction on y–z plane with injection.

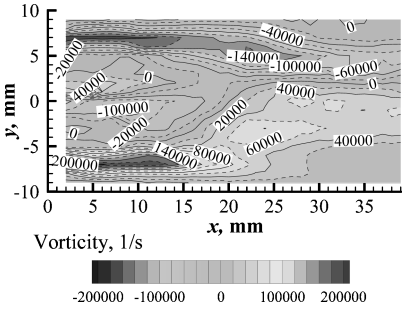

Fig. 13 Streamwise vorticity distribution on x–z plane at z = 4 mm with injection.

to the vortex pair produced by the ramp injector shown in Fig. 11. These isovorticity surfaces departed slightly from each other as they moved downstream.

In the injection case shown in Figs. 12c, 12d, and 14b, another pair of isovorticity surfaces appeared. The outer pair corresponded to the one observed in Fig. 11d, but their centers moved outside the sidewalls of the ramp. The inner pair was not clear in Figs. 11c and 11d. These vortices were produced by the main flow pushed inside between the twin jets by themselves. The contours in the $x = 5$ and 15 mm sections shown in Figs. 12c and 12d indicate that the outer pair was stronger and larger than the inner one. The contours in the $z = 4$ mm plane shown in Fig. 13 show that the outer pair was located outside of the sidewalls of the ramp up to $x = 18$ mm, and then they moved inside. The inner vortices existed up to $x = 18$ mm and then became weaker and more difficult to distinguish in this plane as they moved further downstream. Comparing the cases with and without injection, we can see that the streamwise vortices produced in the injection case were stronger than those in the noninjection case. The twin jets served as aerodynamic extensions of the ramp and intensified the streamwise vortices.

E. Discussion

In the present research, the distributions of velocity around a ramp injector with and without injection were measured with two objectives. One was for clarification of the characteristics of streamwise vortices that interacted with a swirl in each jet in previous research.[12] Another was for clarification of the influence of twin jets on the streamwise vortices.

The existence of a pair of streamwise vortices had been shown in many previous studies[13] where there was one injection hole on the base of the ramp injector. However, there was no information of the streamwise vortices around the ramp injector with two holes on its base. Thus, it was not clear how the streamwise vortices around the ramp interacted with the swirl in each jet in previous research.[12] In the present research, the velocity distribution around the ramp injector indicated that two pairs of the streamwise vortices were produced and that the center of the outer vortices was located outside of the sidewall of ramp. It is considered that this information is useful in modeling the flowfield around a ramp injector with two holes.

In the case without injection, only a pair of streamwise vortices exists behind the ramp near the lower wall. Note the difference of the position and the strength of the streamwise vortices between the two cases. When the injection was stopped, the height and strength of the streamwise vortices decreased. In this case, the streamwise vortices of ramp may not be expected to enhance mixing in the main flow, but mainly to transport the momentum of the main stream to the boundary layer and suppress large separation.

It is also important to compare the ramp injectors with one and two holes. In the present case, the interaction between the outer and the inner streamwise vortices produced flow moving upward and outward. The injectant was mainly transported by this flow and spread widely. On the other hand, the flow moving only upward was produced on the centerline of the base of the ramp with single hole because of the interaction between the pair of vortices. The distance between the centers of these streamwise vortices is shorter than that of the outer pair of streamwise vortices in the present study. Thus, it is considered that the penetration of the injectant is better in the

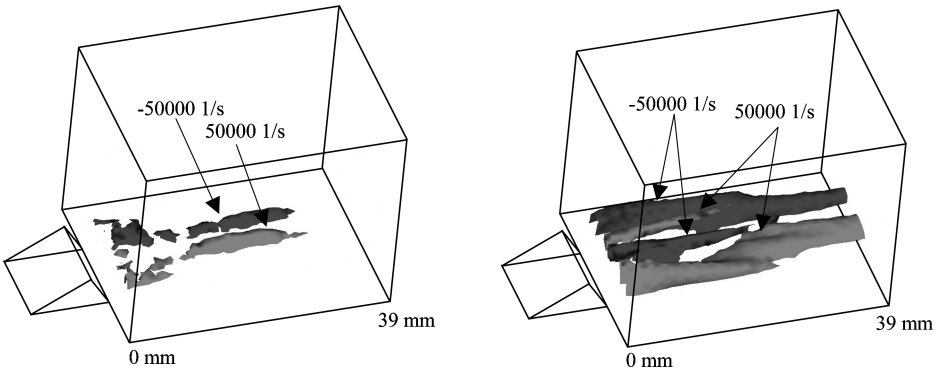

a) Without injection **b) With injection**

Fig. 14 Contour surfaces of streamwise vorticity.

single-hole case and that the lateral expansion of that is better in the twin-hole case.

IV. Conclusions

The structure and characteristics of the streamwise vortices produced by a ramp injector in a Mach 2.35 airstream were experimentally investigated. Three-dimensional distributions of velocity and vorticity were measured by particle image velocimetry for the noninjection and injection cases. The following conclusions were obtained.

In the noninjection case, a pair of vortices was produced around the ramp injector and the centers of these vortices were located behind the ramp injector.

In the injection case, two pairs of vortices were observed around the ramp injector. The centers of one pair were outside the sidewalls of the ramp and their directions of rotation were the same as those in the noninjection case. The other pair lay near the central plane and higher than the trailing edge of the ramp.

The characteristics of the streamwise vortices generated by the ramp injector were significantly modified by the injected jets not only quantitatively, but also qualitatively.

Acknowledgments

The results were visualized with the visualizing software POST_KUN developed by Fujii Laboratory of University of Tokyo. This work was supported by the Ministry of Education, Culture, Sports, Science, and Technology (Grant in Aid for Scientific Research (A) (2) 15206090) and supported by Research Fellowships of the Japan Society for the Promotion of Science through Grant 17004966.

References

[1]Chinzei, N., Masuya, G., Komuro, T., Murakami, A., and Kudou, K., "Spreading of Two-Stream Supersonic Turbulent Mixing Layers," *Physics of Fluids,* Vol. 29, No. 5, 1986, pp. 1345–1347.

[2]Papamoschou, D., and Roshko, A., "The Compressible Turbulent Shear Layer: An Experimental Study," *Journal of Fluid Mechanics,* 1988, Vol. 197, pp. 453–477.

[3]Swithenbank, J., and Chigier, N. A., "Vortex Mixing for Supersonic Combustion," *Proceedings of the 12th International Symposium on Combustion*, Combustion Inst. Pittsburgh, PA, 1968, pp. 1153-1162.

[4]Northan, B. G., Greenberg, I., Byington, C. S., and Capriotti, D. P., "Evaluation of Parallel Injector Configurations for Mach 2 Combustion," *Journal of Propulsion and Power*, Vol. 8, No. 2, 1992, pp. 491–499.

[5]Seiner, J. M., Dash, S. M., and Kenzakowski, D. C., "Historical Survey on Enhaced Mixing in Scramjet Engines," *Journal of Propulsion and Power*, Vol. 17, No. 6, 2001, pp. 1273–1286.

[6]Cutler, A., and Johnson, C., "The Use of Swirling Jet Pairs to Provide Rapid Fuel Penetration in Scramjet Combustors," AIAA Paper 95-0099, Jan. 1995.

[7]Wilson, M. P., Bowersox, R. D., and Glawe, D. D., "Experimental Investigation of the Role of Downstream Ramps on a Supersonic Injection Plume," *Journal of Propulsion and Power*, Vol. 15, No. 3, 1999, pp. 432–439.

[8]Ichikawa, N., Choi, B., Nakajima, T., Masuya, G., and Takita, K., "Behavior of Pseudo-Shock Wave Produced by Heat Addition and Combustion," AIAA Paper 2002-5245, Sept.– Oct. 2002.

[9]Waitz, I., Marble, F., and Zukoski, E., "Investigation of a Contoured Wall Injector for Hypervelocity Mixing Augmentation," *AIAA Journal*, Vol. 31, No. 6, 1993, pp. 1014–1021.

[10]Marble, F., Zukoski, E., Jacobs, J., Hendricks, G., and Waitz, I., "Shock Enhancement and Control of Hypersonic Mixing and Combustion," AIAA Paper 90-1981, July 1990.

[11]Ton, V. T., Karagozian, A. R., Marble, F. E., Osher, S. J., and Engquist, B. E., "Numerical Simulations of High Speed Chemically Reacting Flow," *Theoretical and Computational Fluid Dynamics,* Vol. 6, No. 2-3, 1994, pp. 161–179.

[12]Hirose, K., Yaguchi, H., Suzuki, K., Takita, K., and Masuya, G., "Mixing of Twin Supersonic Swirling Jets Injected from a Ramp," *Journal of the Japan Society for Aeronautical and Space Science*, Vol. 52, No. 600, 2004, pp. 16–22 (in Japanese).

[13]Donohue, J. M., McDaniel, J. C., Jr., and Haj-Hariri, H., "Experimental and Numerical Study of Swept Ramp Injection into a Supersonic Flowfield," *AIAA Journal*, Vol. 32, No. 9, 1994, pp. 1860–1867.

[14]Melling, A., "Tracer Particle and Seeding for Particle Image Velocimetry," *Measurement Science and Technology*, Vol. 8, No. 12, 1997, pp. 1406–1416.

[15]Yoshida, S., Kato, F., Takita, K., and Masuya, G., "Effects of Swirl on Supersonic Jets," *Proceedings of the 39th Conference on Aerospace Propulsion*, Japan Society for Aeronautical and Space Sciences, Tokyo, 1999, pp. 30–35 (in Japanese).

[16]Henderson, C. B., "Drag Coefficients of Spheres in Continuum and Rarefied Flows," *AIAA Journal*, Vol. 14, No. 6, 1976, pp. 707–708.

[17]Kitamura, E., Matsumoto, M. Koike, S., and Masuya, G., "PIV Measurement of Supersonic Swirling Jet," *Proceedings of the 30th Symposium on Visualization*, Visualization Society of Japan, Tokyo, 2002, pp. 189–192 (in Japanese).